



Impact of morphology on the oxygen evolution reaction of 3D hollow Cobalt-Molybdenum Nitride

Hongqi Chu, Dan Zhang, Bowen Jin, Min Yang*

MIIT Key Laboratory of Critical Materials Technology for New Energy Conversion and Storage, School of Chemistry and Chemical Engineering, Harbin Institute of Technology, Harbin, 150001, China

ARTICLE INFO

Keywords:

Cobalt-Molybdenum Nitride
3D hollow structure
Oxygen evolution reaction
ZIF-67 template

ABSTRACT

The oxygen evolution reaction (OER) is an essential process for water electrolysis and to realize the scalability of renewable energy sources. In this work, a strategy is developed to fabricate anisotropic metallic Cobalt-Molybdenum Nitride materials combining hollow 3D structures and 2D nanosheets which result highly active OER electrocatalysts. The sample structure and morphology is investigated to derive its formation process following the synthesis strategy relying on the ligand-metal interactions of metal-organic framework (ZIF-67 and Mo-aMOF). Three different sample morphologies with large specific surface areas are obtained by changing the water and 2-methylimidazole contents. After ammonification in NH_3 , the morphologies and the specific surface areas of the samples are preserved. The electronic structure can also be adjusted to regulate electron density of Co and Mo by N-doping. These Co-Mo binary metals offer a viable way for realizing the electronic transfer between the different components, as demonstrated by XPS. Taking advantage from the above features, the as-obtained electrocatalyst exhibits a high catalytic activity and long-term cyclic stability for OER with low overpotential (η_{10} is 294 mV).

1. Introduction

The long-term use of fossil fuels has accelerated their consumption and resulted in the problematic environmental pollution. Water splitting is an effective energy conversion process for replacing fossil fuels within a short time ideally resulting in zero pollution [1,2]. The process of water electrolysis needs the use of stable and inexpensive electrocatalysts that are highly active to promote water splitting by overcoming the reaction kinetics. Compared to the hydrogen evolution reaction (HER), the limiting factor of the oxygen evolution reaction (OER) is the speed control step due to its tedious basic steps and sluggish kinetics [3]. Developing hybridized binary catalysts with optimized micro/nanostructure, favoring the electron transfer between the different components by the specific microscopic coordination structure, is an effective pathway to enhance the electrocatalytic activity [4–6]. In this context, 3D hollow nanostructures coupled with 2D nanosheets have conferred to the electrocatalysts a particularly high activity thanks to the presence of abundant electrochemically active sites and mass diffusion pathways to transport relevant species (by the charge and release of bubbles) [7,8].

Metal-organic frameworks (MOFs), consisting of inorganic metal ions or clusters coordinated to organic molecules, are an original class

of porous materials possessing specific properties including structural flexibility, incredibly high internal surface area and ultrahigh porosity. Attractively, heterogeneous structures can be easily realized by poly-metallic MOFs [9]. As a promising MOF material, ZIF-67, combining 2-methylimidazole and cobalt ions has been widely applied for sensing, energy conversion and storage and catalysis [10–12]. In particular, NiCoP/C and $\text{Co}_3\text{O}_4/\text{CoMoO}_4$ have been synthesized via ZIF-67 template and used as OER electrocatalysts with overpotential of 330 mV and 318 mV (at current density of 10 mA cm^{-2}), respectively [13,14]. In most cases, ZIF-67 is often used as a precursor and need to be synthesized separately because of its formation process is extremely critical for the environment. This multi-step synthesis can result in reduced energy efficiency. The microscopic coordination between 2-methylimidazole and cobalt, molybdenum ions can be exploited for achieving the formation of binary catalysts, with possibly controlling their morphology and predicting the formation process of an unknown binary compound structure. Besides, transition metal nitride, like cobalt nitride or molybdenum nitride, can provide for a tunable electronic structure and good corrosion resistance, thus allowing to reach excellent HER and OER electrocatalytic activities [15–18].

In this work, we report a shape controlled 3D hollow Co-Mo hybridized binary catalyst via ZIF-67 based on a one-step facile

* Corresponding author.

E-mail address: yangmin@hit.edu.cn (M. Yang).

<https://doi.org/10.1016/j.apcatb.2019.117744>

Received 2 March 2019; Received in revised form 8 May 2019; Accepted 14 May 2019

Available online 15 May 2019

0926-3373/© 2019 Elsevier B.V. All rights reserved.

hydrothermal method. The binary catalyst can generate a particularly strong electron transfer between Co and Mo. A high specific surface area is obtained thanks to the coupling of 3D hollow nanostructures with 2D nanosheets. The synergy between the morphology and composition of the Co-Mo polyhedrons binary heterostructure results in a remarkably high OER activity and stability. Following the NH_3 heat treatment, the optimal Cobalt-Molybdenum Nitride compound exhibits an attractive overall performance comprising an early onset at 1.46 V, an overpotential of 294 mV and achieves a current density of 10 mA cm^{-2} , a Tafel slope of 57 mV dec^{-1} and strong durability around 20 h.

2. Experimental

2.1. Materials

All aqueous chemicals were prepared with high-purity, Molybdenyl acetylacetonate, cobalt nitrate hexahydrate, 2-Methylimidazole, methanol, glycerol, isopropanol and ethanol, purchased from Shanghai Sinopharm Chemical Reagent and used without further purification. The water used in this work was deionized water (DI-water) with resistance of $18.2 \text{ M}\Omega \text{ cm}^{-1}$. Nafion solution (5 wt%) was purchased from Sigma Aldrich.

2.2. Preparation of 3D hollow cobalt molybdenum composites

In a typical synthesis, 0.87 g cobalt nitrate hexahydrate and 0.133 g molybdenyl acetylacetonate were dissolved in 10 mL methanol under strong stirring for 1 h at room temperature. 2 g 2-methylimidazole (2-MIM) was added to the above solution and continued stirring for 1 h. The solution was transferred into a Teflon-lined stainless-steel autoclave which contained a mixed solutions made of 20 mL distilled water, 15 mL glycerol, 10 mL isopropanol and 15 mL ethanol with agitated stirring for 0.5 h, maintained at 180°C for 48 h. After cooling, the product was collected by centrifugation and washed several times with DI water and ethanol, dried under vacuum at 130°C overnight (denoted as Co-Mo-PHP). The product was followed annealed at 400°C for 1 h under a NH_3 atmosphere at a ramping rate of 4°C min^{-1} to form hollow 3D Cobalt-Molybdenum Nitride material (denoted as Co-Mo-N-PHP). When only the water content was changed to 10 mL and the 2-MIM content was changed to 1.6 g, a spherical structure was obtained (denoted as Co-Mo-PHS and Co-Mo-N-PHS). When the 2-MIM content was more than 2 g and other synthetic conditions were similar as the preparation of Co-Mo-PHP and Co-Mo-N-PHP. Then samples dominated by

ZIF-67 would be obtained (denoted as ZIF-67-PHP and ZIF-67-N-PHP).

2.3. Characterization methods

Morphological characterizations were performed by high resolution transmission electron microscopy (HRTEM, 2100 F, JEOL, Japan) and field-emission scanning electron microscopy (FE-SEM, Supra TM55, Zeiss). The pore size distribution and specific surface area of the material was determined by BET analysis (Brunauer-Emmett-Teller, 3H-2000PS1, China). An X-ray diffractometer (XRD, D8-Advance, Bruker) equipped with Cu K α radiation ($\lambda = 0.15406 \text{ nm}$) was used to derive the crystalline structure of the as-prepared samples. X-ray photoelectron spectroscopy (XPS) was used to investigate the chemical and elemental compositions of the catalysts surface (ESCALAB 250Xi by Thermo).

2.4. Electrochemical measurements

The electrochemical properties were evaluated on an electrochemical workstation (CHI 760D, Chen Hua Ltd, China) in a conventional three-electrode configuration in 1 mol L^{-1} KOH electrolyte with Ag/AgCl reference electrode and carbon rod counter electrode. For the fabrication of the working electrode, the as-synthesized samples (4 mg) and $50 \mu\text{L}$ Nafion solution (5 wt%) were mixed in 1 mL of deionized water: ethanol solution (7:3) and ultrasonicated for 1 h to generate a homogeneous slurry. Then the suspension ($5 \mu\text{L}$) was dropped onto the glassy carbon rotating disk electrode surface (3 mm , 0.07 cm^2). The iR-corrected polarization curves were recorded in O_2 pre-saturated 1 mol L^{-1} KOH solution by linear sweep voltammetry (LSV) with scan rate of 5 mV s^{-1} . Tafel plots are derived from the equation $Z = b \log(j) + a$, where b is Tafel slope and j is the current density. Electrochemical impedance spectroscopy (EIS) measurements were operated with an AC amplitude applied of 5 mV and frequency from 0.01 – 100 kHz . Electrochemical measurements of the double-layer capacitance were carried out via cyclic voltammetry (CV) in the potential range from 0.17 to 0.27 V vs Ag/AgCl with different scan rates of 2, 4, 6, 8, and 10 mV s^{-1} , respectively. By plotting the j ($j = j_a - j_c$) at the potential of 0.22 V vs Ag/AgCl against the scan rate, the linear slope C_{dl} is used to evaluate the electrochemical surface area (ECSA).

3. Results and discussion

3D hollow Co-Mo composites are fabricated via hydrothermal synthesis without template. In brief, cobalt nitrate hexahydrate and

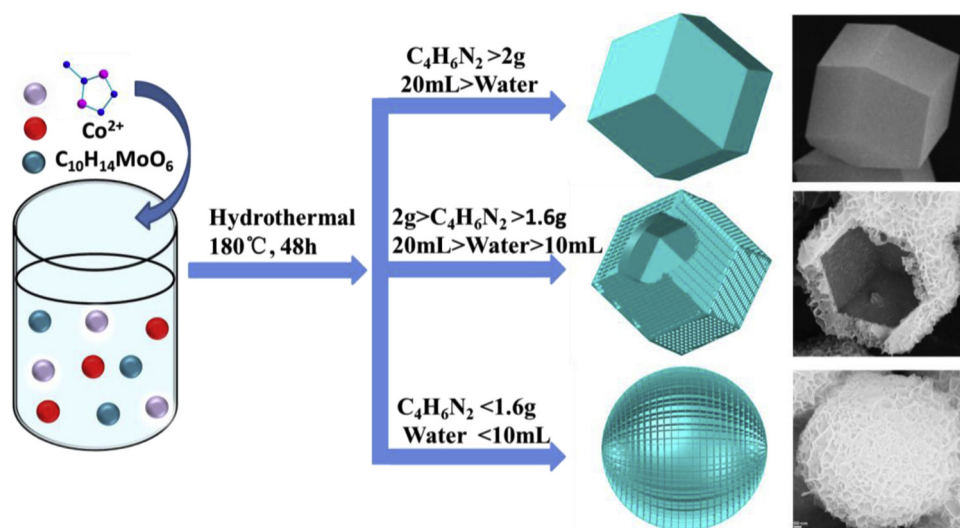


Fig. 1. Illustration of the fabrication process of samples (ZIF-67-PHP, Co-Mo-PHP and Co-Mo-PHS) with different morphologies.

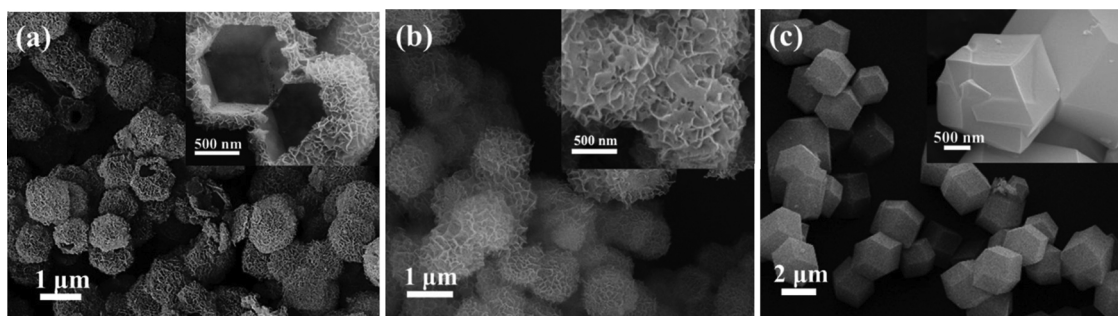


Fig. 2. The SEM images of samples with different morphologies. (a) Co-Mo-PHP, (b) Co-Mo-PHS, and (c) ZIF-67-PHP.

molybdenyl acetylacetonate are used as cobalt and molybdenum sources, and 2-methylimidazole (2-MIM) is used as a ligand. Fig. 1 displays the forming processes of the different morphologies for materials synthesized through two-step processes. Results show that the final products morphology is strongly affected by the water and 2-MIM contents. As the water content increases, the morphology of the particles morphology changes from spherical to polyhedral and at the same time, the two-dimensional nanosheets grow in the outer layer. Meanwhile, 2-MIM favors the reaction of molybdenum ions with cobalt ions to formulate the ZIF-67. If the 2-MIM content is too high (over 2 g), the product will only contain ZIF-67. Under the optimum conditions, a shape controllable hollow 3D cobalt–molybdenum polyhedron with 2D nanosheets is formed and annealed in a NH_3 atmosphere at 400 °C for 1 h.

SEM images of the Co-Mo-PHP were shown in Fig. 2a, showing that hollow structures and abundant nanosheets are formed after the reaction at the sample surface. Moreover, the morphology of the Co-Mo-PHP is similar to the ZIF-67 with an average size of about 1.2 μm. The structure features a 3D hollow skeleton decorated by 2D nanoplates (inset in Fig. 2a), which enable the exposure multiple active sites and is beneficial for the adsorption as well as activation of the reactants and intermediate products. In addition, the 2D nanoplates are in contact with each other, which is beneficial to ensure good electrical conductivity. At the initial stage of this reaction process, cobalt ions released from Co-glycerate sphere reaction with the 2-MIM promote the formation of the 3D hollow framework ensuring a large specific surface area. Meanwhile, the cobalt element with the help of molybdenum ions forms 2D nanoplates on the outer surface of the structure. Note that the morphology of the products is well correlated with the 2-MIM amount in water. The water content influences the cobalt ions concentration and the 2-MIM amount determines whether the final product possess a morphology similar to ZIF-67. When the water content is between 15 and 20 mL and the amount of 2-MIM is between 1.6 and 2 g, the sample morphology is rhombododecahedral, which is consistent with ZIF-67 (inset of Fig. 2a). Fig. 2b shows separately the morphology of the as-obtained products, when an insufficient amount of water (< 15 mL) and 2-MIM (< 1.6 g) are used; the cobalt ions concentration in the reaction system cannot thus meet the requirement to form ZIF-67. The morphology of product is spherical with nanoplates at the surface emerging from Co-glycerate spheres. When the 2-MIM amount exceed 2 g, the final product is ZIF-67 (Fig. 2c) because all of cobalt ions are bonded to the 2-MIM.

The forming processes of Co-Mo-PHP were showed in Fig. 3. The cobalt molybdenum precursor was synthesized by a facile hydrothermal method. As shown in the illustration, cobalt ions are reacted with glycerol to form Co-glycerate sphere firstly [19]. Then, the Co precursor which is easy to dissolve in water released ions slowly in aqueous solution. It means the release rate of cobalt ions can be controlled by water content and affect the final morphology of the product (Fig. S1). With the increase of water contents, the morphology of the sample changes from spherical to polyhedral, and along with the two-dimensional nanosheets grew in the outer layer. Fig. S2 showed the SEM

images of the samples in different time reactions can prove that conclusion, representing a polyhedral morphology with a solid sphere inside. And the phenomenon also has been verified by TEM image (Fig. S4c). The shape of the samples is same as the ZIF-67, due to 2-methylimidazole preceded molybdenum ions to react with cobalt ions to formulate the ZIF-67 (Fig. S3d). 2-methylimidazole can react with cobalt and molybdenum, respectively (Fig. 3b) [20]. While excessive amount of 2-methylimidazole will inhibit molybdenum ions to participate in the reaction due to all of cobalt ions are occupied by 2-methylimidazole. This can be proved by the atoms ratio of cobalt and molybdenum in Table S1 and Fig. S14. The increased proportion of cobalt and molybdenum arises from the stronger coordination ability of cobalt than molybdenum in the presence of 2-methylimidazole, and thus giving rise to the change in morphology from spherical to polyhedral. If the content of 2-methylimidazole is too high (over 1.6 g), the product will only form ZIF-67, as shown the SEM images in Fig. S3f. This method regulates samples synthesis via controlling ligand-metal interactions, based on the competition of different coordination sites of metal elements/clusters with useful ligands.

After ammonification, the sample shape remains polyhedral with micrometer size Co-Mo-PHP particles, shown in Fig. 4a. The interior porous structure of Co-Mo-N-PHP was further observed by high resolution TEM (Fig. 4b). The porous structure is beneficial for the OER electrocatalysis in order to shorten charge and mass transfer distance and to maximize the exposition of active sites [21,22]. The Co-Mo-N-PHP particles are rhombododecahedrons in shape with the nanosheets at the edges. Elemental maps of N, Co and Mo elements in one Co-Mo-N-PHP article indicates the successful fabrication of the Co-Mo bimetal composites. Fig. 4c shows that the Co-Mo-N-PHP catalyst features an interplanar spacing of 0.214 and 0.225 nm assigned to the (200) and (111) crystal planes of CoN and 0.28 and 0.37 nm assigned to the (002) and (101) crystal planes of MoN. In addition, we observe the presence of lattice fringes corresponding to Co_2N , Co_4N and Co_2C . The HRTEM images (Figs. 4c and S4) show that the granules are assembled on their surface. The presence of the porous carbon skeleton is convenient for maintaining the integrity of the structure after heat treatment and for ensuring the performance stability of the electrocatalyst. Besides, highly conductive porous carbon skeleton provides for the carrier and transport network to promote the charge transfer during the electrochemical reactions. The interconnected granules provide for efficient oxygen evolution reaction sites. Furthermore, the nanosheets act as receiving amplifiers, which enable to easily releasing the evolved gas bubbles through effective pathways. Overall, this porous carbon skeleton, granules and nanosheets are integrated into a full reaction system with good electrical contacts and mechanical properties.

The crystalline structure of the Co-Mo-N-PHP electrocatalysts was further investigated by XRD (Fig. S5a). The wide peak located at 26.6° is related to graphitic carbon (JCPDS, No. 26-1079). Obviously, it was mainly derived from the conversion of 2-MIM and other organic compounds including the acetyl group following the heat treatment. That is, the presence of 2-MIM and the acetyl groups can provide a way to increase the conductivity of the sample, thereby improving the

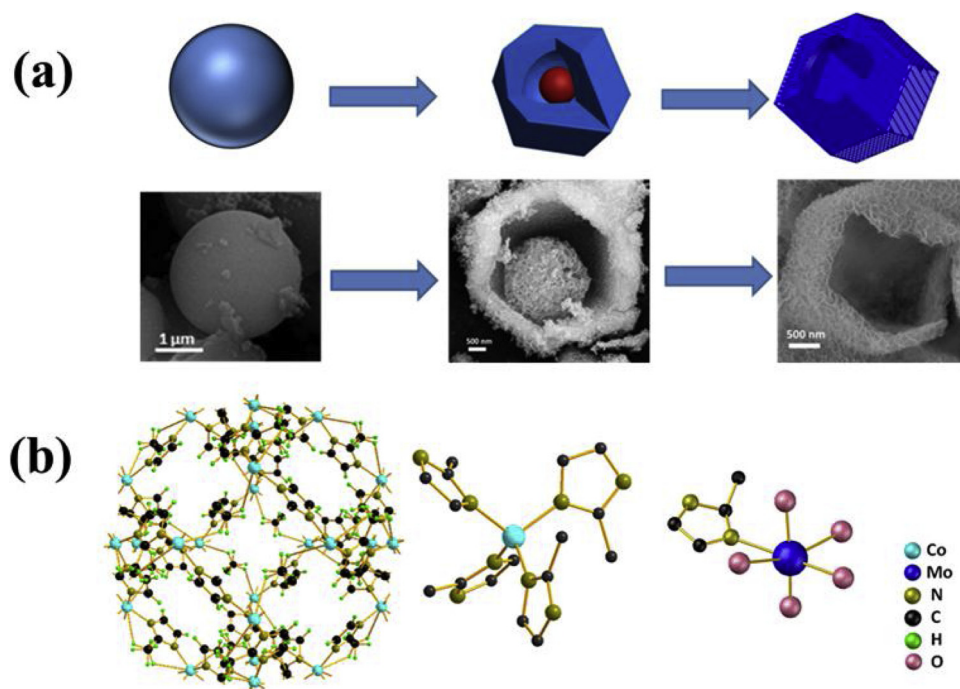


Fig. 3. (a) The illustration of formation process of Co-Mo-PHP, and (b) coordination modes of ZIF-67 and Mo-MOF.

electrochemical performance of the material. The several diffraction peaks located at $2\theta = 36.2^\circ$, 42.2° and 61.3° are assigned to (111), (200) and (220) planes of CoN (JCPDS, No. 16-0116). The peaks located at $2\theta = 36.2^\circ$ and 65.1° are assigned to (200) and (211) planes of MoN (JCPDS, No. 25-1367). Its presence can possibly improve the catalyst conductivity. As shown in Fig. S5b, the XRD pattern of ZIF-67-PHP reveals that the main diffraction peaks coincide with ZIF-67 (JCPDS,

No. 85-1179). Noticeably, the peak intensity of ZIF-67-PHP is enhanced by the presence of molybdenum.

X-ray photoelectron spectroscopy (XPS) measurements were conducted to get the detailed surface electronic state and elemental compositions of the Co-Mo-PHP and Co-Mo-N-PHP (Figs. 5 and S6). The composite contains C, N, O, Co and Mo elements (Fig. S6a). We observe that the Co 2p peak components (Fig. 5a) at lower binding energy (BE)

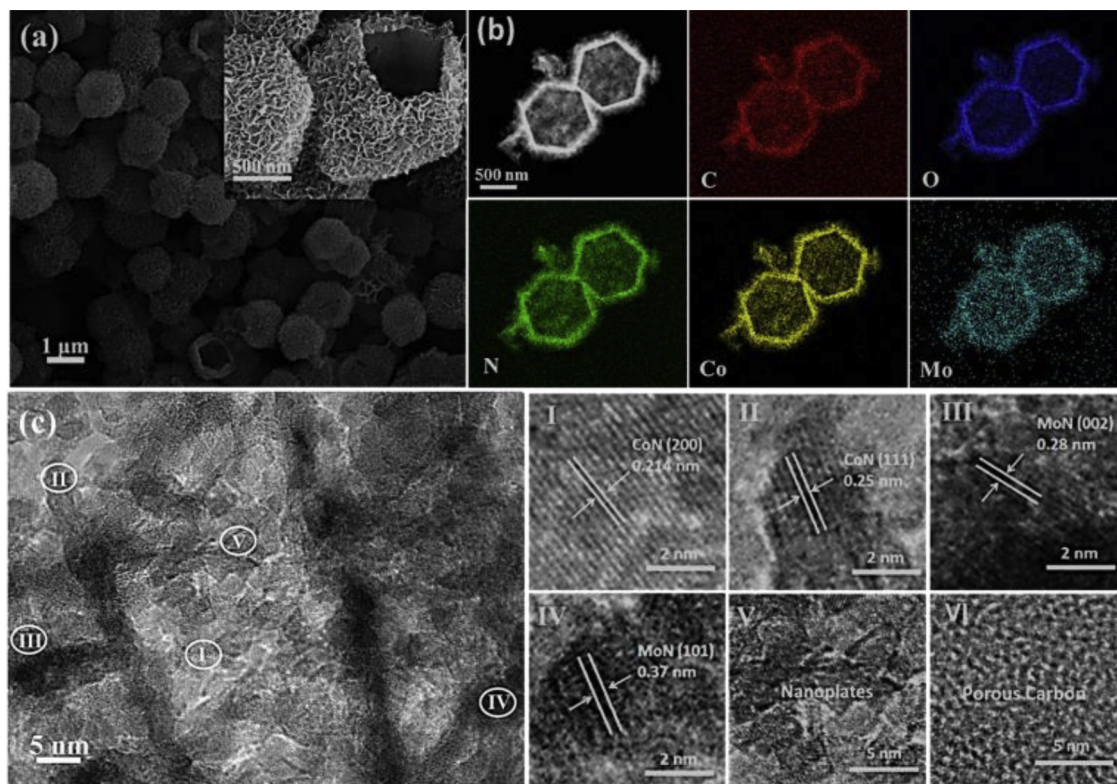


Fig. 4. Morphological characterization of Co-Mo-N-PHP: (a) SEM images of Co-Mo-N-PHP, (b) TEM images and elemental mappings of the hollow 3D Co-Mo-N-PHP, (c) TEM images of Co-Mo-N-PHP (VI from Fig. S4a).

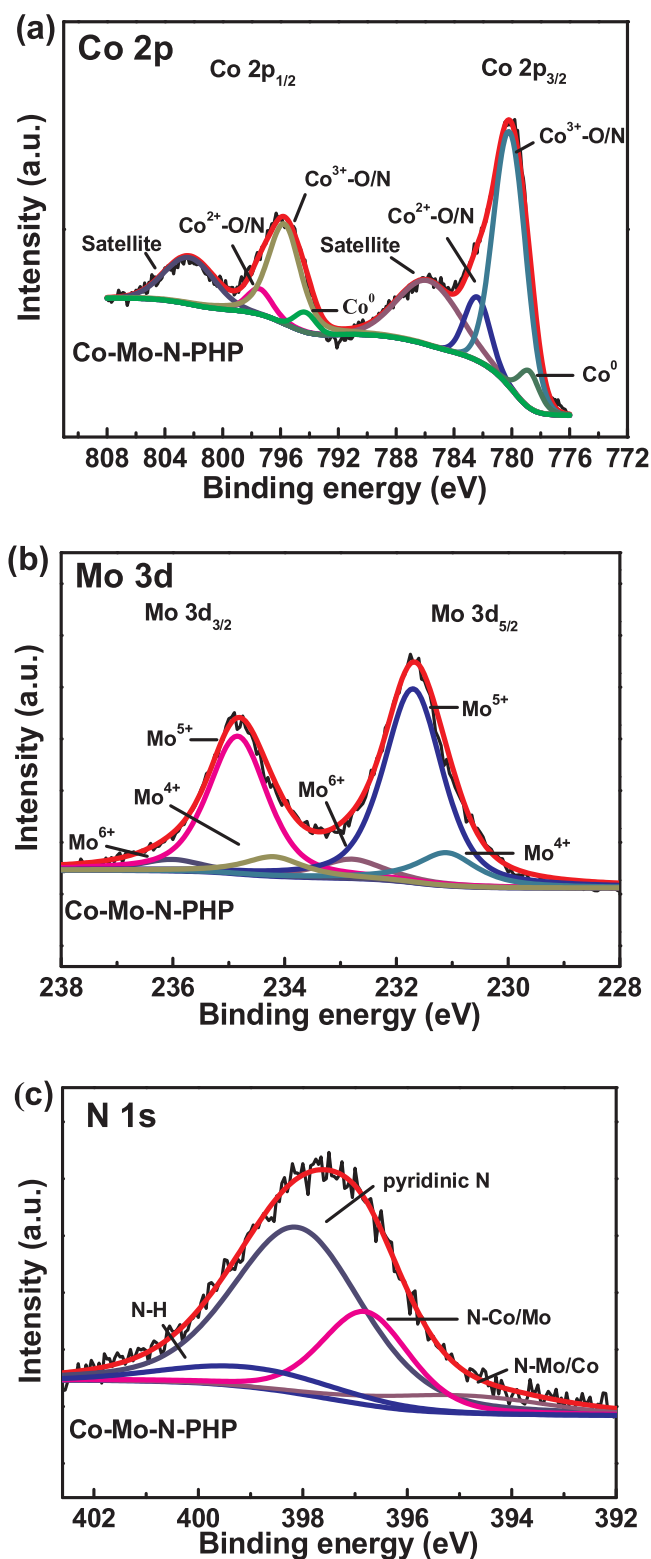


Fig. 5. XPS spectra of Co-Mo-PHP and Co-Mo-N-PHP catalysts: (a) Co 2p, (b) Mo 3d, (c) N 1s.

obviously increase. This means that the electron density on Co increases, mainly due to the deviation of the average electron state of Co to the low valence side, indicating the availability of Co centers to the whole charge density distribution [23]. The Mo 3d peak position (Fig. 5b) slightly moves to higher BEs due to the electron transfer between Co and Mo (from 230.2–231.75 eV). This phenomenon also

occurs for the N spectrum peak which shifts from 396.6–397.5 eV. Beyond that, compared to the peak position of the elemental Co, Mo and N, the Co 2p and Mo 3d peak positions are positively shifted from 778.1 and 229.5 eV–779.8 eV and 231.75 eV, and the N 1s peak (Fig. 5c) is negatively shifted from 398.4 eV to 397.5 eV. This implies that electron transfer occurs between cobalt, molybdenum and nitrogen atoms, resulting in for Co–N and Mo–N covalent bondings formation [24,25]. Furthermore, after ammonization, the nitrogen content increases significantly, which proves that nitrogen doping can be used to regulate the electronic structure of metals.

The C 1s spectrum of the Co–Mo–N–PHP (Fig. S6b) shows three components peaks at 284.5, 285.9 and 288.3 eV, ascribed to C–C/C–H, C–N and C=O/C–O, respectively [26–28]. Here, the peak related to C–N (at 285.9 eV) confirms the N-doping of the carbon matrix. The Co 2p spectrum obtained from the Co–Mo–N–PHP sample (Fig. 5a) is fitted by four components, corresponding to Co^{2+} -O/N (782.5 and 797.5 eV), Co^{3+} -O/N (780.1 and 795.7 eV), Co^0 (778.8 and 794.3 eV), and a shake-up satellite peak (785.8 and 802.3 eV) [29–31]. The presence of the Co–O/N bonds suggests that the Co is coordinated to both O or N ions. Meanwhile, the presence of Co^0 , which is reduced by NH_3 , is beneficial to enhance the activity versus the OER by improving the electronic conductivity [32]. The Mo 2p spectrum of the Co–Mo–N–PHP (Fig. 5b) features three components, attributed to Mo^{4+} (234.2 and 231.1 eV), Mo^{5+} (234.8 and 231.7 eV) and Mo^{6+} (236 and 232.8 eV), respectively [33–35]. The corresponding HR-XPS N 1s spectrum of the Co–Mo–N–PHP is shown in Fig. 5c, showing a main component at 398.1 eV attributed to pyridine N which is beneficial for the OER and ORR reactions [36,37]. The components at 394.3 eV and 396.8 eV are ascribed to Co/Mo–N bonds and the peak at 399 eV is ascribed to N–H bonds [30,38]. The formation of metal nitrides and the presence of N–H bonds formed by the incomplete dissociation of NH_3 , indicate that N ions are abundant at the sample surface. Overall, XPS results indicate that the final product mainly consists of cobalt nitride and molybdenum nitride and that carbon is successfully N-doped. The N1 s XPS spectrum of the Co–Mo–PHP catalyst (Fig. S6d) clearly shows a peak centered at 396.6 eV ascribed to $\text{C}=\text{N}-\text{C}$ (M–N) bonds originating from the 2-MIM. The peak component at 397 eV is ascribed to M–N bonds, resulting from the substitution of O atoms in the crystal lattice by N atoms. This substitution can facilitate the transport of charge carriers and can modify the C electronic structure. This also implies that there are many oxygen vacancies in the sample surface, which is favorable for improving the catalytic activity [39,40]. Furthermore, by comparing the two peak areas, we see that there are many uncoordinated sites on the 2-MIM ring, meaning that there is a high density of defects. Fig. S6c and e–f show the high resolution XPS spectra of O 1s, Co 2p and Mo 3d obtained from Co–Mo–N–PHP analysis.

N_2 adsorption-desorption isotherms were carried out to derive the specific surface area (see Table S2) and the pore size (Figs. 6 and S7). Each sample features fourth distinct hysteresis loops in the high pressure region, indicating the mesoporous structure derived from the stacking of 2D layers in the catalyst. The hollow interior coupled with appropriate mesoporous structure is beneficial for the improvement of catalyst performance as it provides plenty of storage space for ions, and facilitates the efficient charge and mass transport. The conductivity of the structure is thus not sensible to defects which improves the desorption rate of products. The specific surface area of the Co–Mo–PHP ($328.5 \text{ m}^2 \text{ g}^{-1}$) is very similar to that of Co–Mo–N–PHP ($318.0 \text{ m}^2 \text{ g}^{-1}$), as shown in Fig. 6a. Obviously, the decomposition of organic matter in the catalyst following the high temperature heat treatment does not cause the collapse of the catalyst structure. This feature plays an important role in improving the activity of the catalyst relying on the large specific surface area to provide a high density of active sites. For both Co–Mo–PHS and Co–Mo–N–PHS catalysts, the specific surface area (Fig. S7a) reduces from $281.5\text{--}161.8 \text{ m}^2 \text{ g}^{-1}$, which is one of the reasons that affect the corresponding electrochemical properties. The pore size distribution plot (Fig. 6b) shows that the pore size distribution is

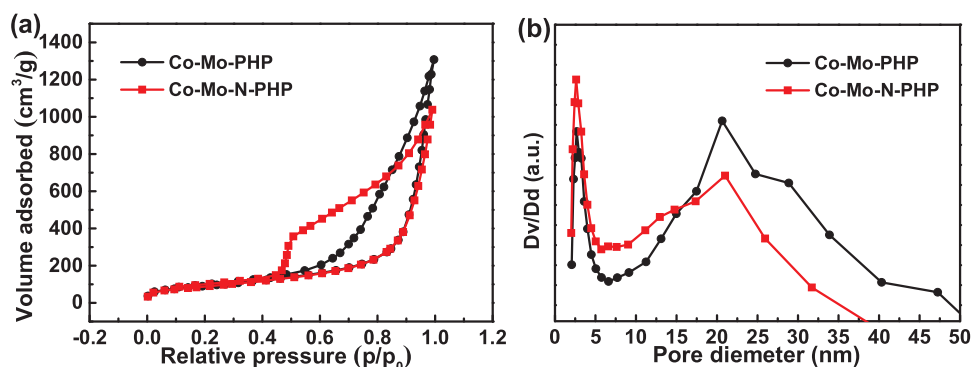


Fig. 6. (a) N₂ adsorption-desorption isotherms of Co-Mo-PHP and Co-Mo-N-PHP. (b) Corresponding Barrett-Joyner-Halenda (BJH) pore size distribution plots of Co-Mo-PHP and Co-Mo-N-PHP.

multimodal, with nanoporous mainly centered at 2.6 nm, and mesopores approximately centered at 21 nm and widely distributed up to 50 nm, demonstrating the formation of a hierarchical pore structure. This may possibly be formed during the pyrolysis process of 2-MIM and acetyl groups, providing at the same time for dense adsorption sites and efficient diffusion for ions and intermediates [41,42].

Line sweep voltammetry was performed to evaluate the electrocatalytic activity of the catalysts toward OER and compare it with the

reference commercial RuO₂ catalyst. Fig. 7a shows the polarization curves iR-corrected to normalize the catalysts loading of 0.269 mg cm^{-2} . As expected, the Co-Mo-N-PHP catalyst displays a lower onset potential and the overpotential at the current density of 10 mA cm^{-2} is 294 mV, while 306 mV for Co-Mo-N-PHS and 361 mV for ZIF-67-N-PHP. This phenomenon is attributed to the hierarchical structure, the high active sites density and the intrinsic activity. It can be concluded that the combination of bimetal metal nitrides would introduce atomic

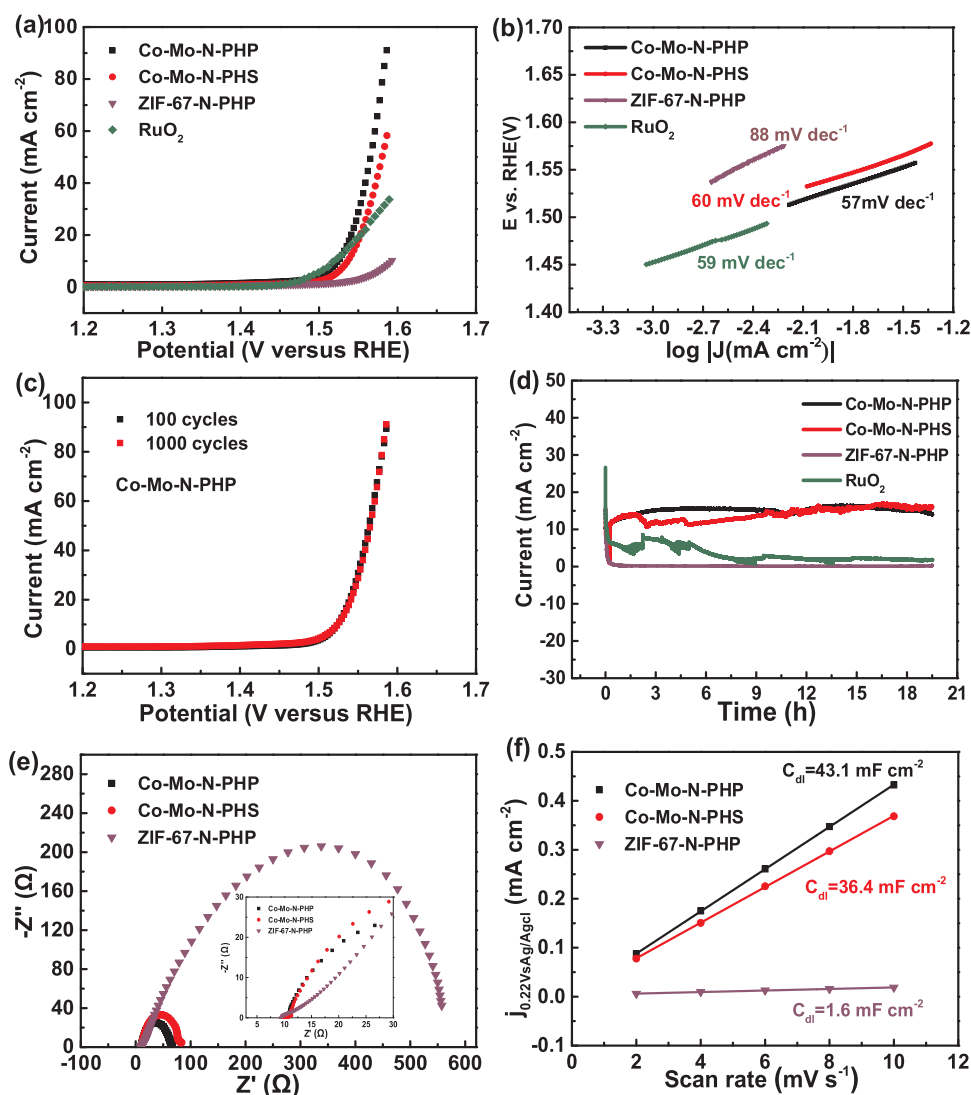


Fig. 7. (a) Polarization curves of Co-Mo-N-PHP, Co-Mo-N-PHS, ZIF-67-N-PHP and RuO₂ for OER at a scan rate of 5 mV s^{-1} under rotation speed of 1600 rpm. (b) Corresponding Tafel plots of Co-Mo-N-PHP, Co-Mo-N-PHS, ZIF-67-N-PHP and RuO₂. (c) Polarization curves of Co-Mo-N-PHP after 100 and 1000 cycles at a sweep rate of 5 mV s^{-1} . (d) Time-dependent current density curves of Co-Mo-N-PHP, Co-Mo-N-PHS, ZIF-67-N-PHP and RuO₂ under a static applied potential of 1.52 V without iR-correction. (e) EIS Nyquist plots of Co-Mo-N-PHP, Co-Mo-N-PHS and ZIF-67-N-PHP electrodes at a constant potential of 0.3 V (simulated equivalent circuit Simplified model in S10). (f) The current density ($j = j_a - j_c$) as a function of the scan rate for different as-obtained catalysts.

arrangements with different microscopic coordination favorably affecting the OER reaction kinetics. Compared to other similar catalysts, the Co-Mo-N-PHP samples show good OER performance in the case of less usage (see Table S3). Meanwhile, from the Tafel plots (Fig. 7b) which are helpful to elucidate the OER reaction kinetics at the electrode/electrolyte interface, it can be concluded that the Co-Mo-N-PHP catalyst exhibits Tafel slope coefficients of 57 mV dec^{-1} , thereby indicating that the catalyst is the limiting factor of the OER kinetics. This confirms that the 3D hollow porous nanostructures coupled with 2D nanosheets is beneficial to the adsorption and conversion of the reactants, and metal nitrides have good electronic conductivity [43,44]. In addition, after 100 and 1000 CV cycles, we observe no significant depletion in the polarization curves of Co-Mo-N-PHP (Fig. 7c), suggesting a high catalytic stability favored by its unique hybrid structure. The i - t curves shown in Fig. 7d illustrate that there is no dramatic change in the current density during continuous operation for about 20 h, further confirming the excellent operation stability. It also should be noted that Co-Mo-N-PHP, Co-Mo-N-PHS and Co-Mo-PHP showed better stability than that of ZIF-67-PHP and RuO_2 . The commercial RuO_2 displays a poor performance in terms of electrocatalytic oxygen evolution stability, which is in line with the reference [45]. That indicates that this unique 3D hollow structure plays a crucial role in the stability of OER. In addition, after 20 h electrochemical stability measurement, no obvious changes were found in SEM and TEM images (see Fig. S12). That is, the remarkable structural stability of catalyst is beneficial to the durability of catalysts in electrocatalytic oxygen evolution. It is also noted Co(OH)_2 was observed from XRD pattern after 20 h electrochemical measurement as shown in Fig. S13, which could be the active species for OER due to the oxidation of Co in alkaline environment [48,49].

To unveil the synergistic effect and explain the high OER activity, electrochemical impedance spectroscopy (EIS) was used to investigate the intrinsic properties of Co-Mo-N-PHP. Two distinct semicircles can be identified in the EIS Nyquist plots in the Fig. 7e. These originate from the high porosity and the large surface area, indicating two distinct time constants [46]. So a two-time-constants equivalent electrical circuit model is used to simulate electrons and charges transfer of the catalysts (Fig. S10). In this scheme, R_s represents the solution resistance, R_1 and CPE_1 are related to the OER charge transfer kinetics and double layer capacitance and R_2 and CPE_2 are related to the oxygen adsorption on the electrode surface [47]. In the Fig. S11, we observe that the diameter of the two circles varies according to the applied potential, indicating that both processes are overpotential-dependent and related to the OER charge-transfer kinetics. The result of EIS analysis indicates the formation of the M-O_{ads} layer, meaning that the adsorption of oxygen intermediates can be considered at the equilibrium. From the fitting of the equivalent circuit, the Mo-Co-N-PHP catalyst shows a small R_{ct} value of 3.9Ω , revealing a good electrical conductivity allowing to enhance the interfacial charge transfer rate. This improves the catalytic activity versus the OER, which relies on highly conductive bimetallic metal nitrides and provides for a high interfacial contact area with the electrolyte.

To better evaluate the active sites density in Co-Mo-N-PHP, the electrochemical surface area (ECSA) was measured by CV in the non-Faradic region at different scan rates (Fig. S8). As shown in Fig. 7f, the double-layer capacitance (C_{dl}) of Co-Mo-N-PHP is 43.1 mF cm^{-2} , meaning that the electrocatalyst has a much larger electrochemical active surface area respect to the Co-Mo-N-PHS (36.4 mF cm^{-2}), Co-Mo-PHP (32.3 mF cm^{-2}) and ZIF-67-N-PHP (1.6 mF cm^{-2}) catalysts. It is worth noticing that the sample without ammonification (Co-Mo-PHP) still showed a large electrochemical active surface area (Fig. S9). This result demonstrates the hollow 3D structure is beneficial for providing enlarged electrochemically active surfaces. The result of Tafel plots, C_{dl} measurements and EIS analysis, indicates that the Co-Mo-N-PHP polyhedrons have an even higher OER activity.

4. Conclusions

In summary, Cobalt-Molybdenum Nitride metallic materials with hollow 3D/2D structure have been successfully synthesized through a facile self-assembly strategy and used as an efficient OER catalyst showing favorable durability. Three different structures and morphologies of the samples were investigated to highlight the synthesis mechanism inspired by the synthesis strategy of ZIF-67. Specifically, the Co-Mo-N-PHP catalyst displays significantly reduced overpotential, is as low as 294 mV and a high durability of about 20 h at the current density of 10 mA cm^{-2} . Most importantly, our strategy can also be applied to regulate the catalyst morphology and an unknown structure can be easily predicted based on our results. This method sensibly enhanced the OER performance thanks to the peculiar combination of ZIF-67-derived 3D hollow cobalt-molybdenum nitride. This unique hybrid 3D/2D structure allows exposing a high density of active sites on the high surface area. Moreover, the intrinsically high activity from binary heterostructure substantially enhances the catalytic activity. Favorable electronic conductivity arises from the presence of metal nitrides which can efficiently enhance the electronic conductivity. This work provides for promising opportunities for the design and preparation of other efficient electrochemical materials like Fe, Zn, Ni and other transition metal elements.

Acknowledgment

This work is financially supported by the National Natural Science Foundation of China (No. 21773046). The authors would like to acknowledge Dr. Peng Chen (Heilongjiang University, China) for XPS measurements.

Appendix A. Supplementary data

Supplementary material related to this article can be found, in the online version, at doi:<https://doi.org/10.1016/j.apcatb.2019.117744>.

References

- [1] I. Roger, M.A. Shipman, M.D. Symes, *Nat. Rev. Chem.* 1 (2017) 0003.
- [2] A. Sivanantham, S. Shanmugam, *Appl. Catal. B: Environ.* 203 (2017) 485–493.
- [3] C.C.L. Mccrory, S. Jung, I.M. Ferrer, S.M. Chatman, J.C. Peters, T.F. Jaramillo, *J. Am. Chem. Soc.* 137 (2015) 4347–4357.
- [4] Q. Zhou, T.-T. Li, J. Qian, Y. Hu, F. Guo, Y.-Q. Zheng, *J. Mater. Chem. A* 6 (2018) 14431–14439.
- [5] X. Wang, L. Yu, B.Y. Guan, S. Song, X.W.D. Lou, *Adv. Mater.* 30 (2018) 1801211.
- [6] X.F. Lu, L. Yu, X.W. Lou, *Sci. Adv.* 5 (2019) eaav6009.
- [7] L. Zhen, J. Zhang, B. Guan, W. Da, L.M. Liu, W.L. Xiong, *Nat. Commun.* 7 (2016) 13065.
- [8] J. Wang, N. Yang, H. Tang, Z. Dong, Q. Jin, M. Yang, D. Kisailus, H. Zhao, Z. Tang, *Angew. Chem. Int. Ed.* 125 (2013) 6545–6548.
- [9] L. Zhang, A. Wu, M. Tian, Y. Xiao, X. Shi, H. Yan, C. Tian, H. Fu, *Chem. Commun.* 54 (2018) 11088–11091.
- [10] H.B. Wu, X.W. Lou, *Sci. Adv.* 3 (2017) eaap9252.
- [11] J. Qin, S. Wang, X. Wang, *Appl. Catal. B: Environ.* 209 (2017) 476–482.
- [12] H. Zhang, J. Nai, L. Yu, X.W. Lou, *Joule* 1 (2017) 77–107.
- [13] P. He, X.Y. Yu, X.W. Lou, *Angew. Chem. Int. Ed.* 129 (2017) 3955–3958.
- [14] L. Zhang, T. Mi, M.A. Ziaee, L. Liang, R. Wang, *J. Mater. Chem. A* 6 (2018) 1639–1647.
- [15] Y. Tong, X. Yu, H. Wang, B. Yao, C. Li, G. Shi, *ACS Catal.* 8 (2018) 4637–4644.
- [16] M. Zhang, Q. Dai, H. Zheng, M. Chen, L. Dai, *Adv. Mater.* 30 (2018) 1705431.
- [17] Z. Chen, Y. Ha, Y. Liu, H. Wang, H. Yang, H. Xu, Y. Li, R. Wu, *ACS Appl. Mater. Interfaces* 10 (2018) 7134–7144.
- [18] Z. Yin, Y. Sun, C. Zhu, C. Li, X. Zhang, Y. Chen, *J. Mater. Chem. A* 5 (2017) 13648–13658.
- [19] L. Yu, B.Y. Xia, X. Wang, X.W. Lou, *Adv. Mater.* 28 (2016) 92–97.
- [20] P. Martián-Zarza, J.M. Arrieta, M.C. Muñoz-Roca, P. Gili, *J. Chem. Soc. Dalton Trans.* 0 (1993) 1551–1557.
- [21] X. Wu, Y. Niu, B. Feng, Y. Yu, X. Huang, C. Zhong, W. Hu, C.M. Li, *ACS Appl. Mater. Interfaces* 10 (2018) 20440–20447.
- [22] S. Cai, Z. Meng, H. Tang, Y. Wang, P. Tsiakaras, *Appl. Catal. B: Environ.* 217 (2017) 477–484.
- [23] C. Yan, G. Chen, X. Zhou, J. Sun, C. Lv, *Adv. Funct. Mater.* 26 (2016) 1428–1436.
- [24] J. Tian, Q. Liu, A.M. Asiri, X. Sun, J. Am. Chem. Soc. 136 (2014) 7587–7590.
- [25] A.P. Grosvenor, S.D. Wik, R.G. Cavell, A. Mar, *Inorg. Chem.* 44 (2005) 8988–8998.

- [26] S.-K. Park, J.K. Kim, Y.C. Kang, *J. Mater. Chem. A* 5 (2017) 18823–18830.
- [27] Z. Chen, Y. Ha, Y. Liu, H. Wang, H. Yang, H. Xu, Y. Li, R. Wu, *ACS Appl. Mater. Interfaces* 10 (2018) 7134–7144.
- [28] J. Jiang, Q. Liu, C. Zeng, L. Ai, *J. Mater. Chem. A* 5 (2017) 16929–16935.
- [29] K.R. Yoon, K. Shin, J. Park, S.-H. Cho, C. Kim, J.-W. Jung, J.Y. Cheong, H.R. Byon, H.M. Lee, I.-D. Kim, *ACS Nano* 12 (2017) 128–139.
- [30] B. Cao, G.M. Veith, J.C. Neufeld, R.R. Adzic, P.G. Khalifah, *J. Am. Chem. Soc.* 135 (2013) 19186–19192.
- [31] Y. Wang, D. Liu, Z. Liu, C. Xie, J. Huo, S. Wang, *Chem. Commun.* 52 (2016) 12614–12617.
- [32] H. Fei, J. Dong, M.J. Arellano-Jiménez, G. Ye, N.D. Kim, E.L. Samuel, Z. Peng, Z. Zhu, F. Qin, J. Bao, *Nat. Commun.* 6 (2015) 8668.
- [33] J.-J. Zhang, X.-L. Sui, G.-S. Huang, D.-M. Gu, Z.-B. Wang, *J. Mater. Chem. A* 5 (2017) 4067–4074.
- [34] J. Jiang, M. Gao, W. Sheng, Y. Yan, *Angew. Chem. Int. Ed.* 128 (2016) 15466–15471.
- [35] G. Zhang, T. Xiong, M. Yan, L. He, X. Liao, C. He, C. Yin, H. Zhang, L. Mai, *Nano Energy* 49 (2018) 555–563.
- [36] D. Geng, Y. Chen, Y. Chen, Y. Li, R. Li, X. Sun, S. Ye, S. Knights, *Energy Environ. Sci.* 4 (2011) 760–764.
- [37] T. Sun, L. Xu, S. Li, W. Chai, Y. Huang, Y. Yan, J. Chen, *Appl. Catal. B: Environ.* 193 (2016) 1–8.
- [38] K. Hada, M. Nagai, S. Omi, *J. Phys. Chem. B* 105 (2001) 4084–4093.
- [39] M. Zhong, Y. Ma, P. Oleynikov, K. Domen, J.-J. Delaunay, *Energy Environ. Sci.* 7 (2014) 1693–1699.
- [40] S.S. Thind, G. Wu, A. Chen, *Appl. Catal. B: Environ.* 111 (2012) 38–45.
- [41] Y.J. Kim, M.H. Lee, H.J. Kim, G. Lim, Y.S. Choi, N.G. Park, K. Kim, W.I. Lee, *Adv. Mater.* 21 (2009) 3668–3673.
- [42] Y. Ren, L.J. Hardwick, P.G. Bruce, *Angew. Chem. Int. Ed.* 122 (2010) 2624–2628.
- [43] C. Ray, S.C. Lee, B. Jin, A. Kundu, J.H. Park, S.C. Jun, *J. Mater. Chem. A* 6 (2018) 4466–4476.
- [44] K. Xu, P. Chen, X. Li, Y. Tong, H. Ding, X. Wu, W. Chu, Z. Peng, C. Wu, Y. Xie, *J. Am. Chem. Soc.* 137 (2015) 4119–4125.
- [45] S. Fu, J. Song, C. Zhu, G. Xu, K. Amine, C. Sun, X. Li, M.H. Engelhard, D. Du, Y. Lin, *Nano Energy* 44 (2018) 319–326.
- [46] Y.-F. Xu, H.-S. Rao, X.-D. Wang, H.-Y. Chen, D.-B. Kuang, C.-Y. Su, *J. Mater. Chem. A* 4 (2016) 5124–5129.
- [47] M. Fang, W. Gao, G. Dong, Z. Xia, S. Yip, Y. Qin, Y. Qu, J.C. Ho, *Nano Energy* 27 (2016) 247–254.
- [48] X. Shi, A. Wu, H. Yan, L. Zhang, C. Tian, L. Wang, H. Fu, *J. Mater. Chem. A* 6 (2018) 20100–20109.
- [49] C. Chen, A. Wu, H. Yan, Y. Xiao, C. Tian, H. Fu, *Chem. Sci.* 9 (2018) 4746–4755.